Coupled phonons in twisted bilayer graphene

N. Girotto [1], L. Linhart [2], and F. Libisch [2]
[1] *Centre for Advanced Laser Techniques, Institute of Physics, 10000 Zagreb, Croatia*
[2] *Institute for Theoretical Physics, TU Wien, 1040 Vienna, Austria*

(Received 9 March 2023; revised 13 September 2023; accepted 14 September 2023; published 12 October 2023)

Stacking two layers of two-dimensional materials slightly twisted relative to each other causes significant alternations of the physical properties of the resulting bilayer. For graphene, at the right twist angle, the electronic band structure features a flat band at the Fermi level that gives rise to interesting many-body physics such as correlated insulators or superconducting states. Likewise, a finite twist angle modifies the phonon band structure. A reciprocal space continuum model including lattice reconstruction due to relaxation allows us to investigate the continuous evolution of the phonon band structure with twist angle. At intermediate angles, we find a complicated structure of the phonon density of states around the frequency of the layer breathing mode, that is substantially broadened by the moiré-induced interaction with the acoustic phonon branches. We infer optical activities and suggest Raman experiments to validate our predictions. Our results suggest that suitably twisting structures may manipulate both phonon and electron properties of such a system, and thus set the stage to test electron-phonon contributions to the observed correlated states.

DOI: 10.1103/PhysRevB.108.155415

I. INTRODUCTION

The potential of vertically stacking two-dimensional (2D) materials to form heterostructures [1,2] has started to attract interest soon after the first isolation of single-layer graphene [3]. With a growing number of new materials, which can be isolated as 2D single- or few-atom layers [2,4] and steadily improving experimental control over these materials, the plethora of possible stacking combinations creates a vast playground for materials science research. The observation of superconductivity [5] close to 1.1° rotated twisted bilayer graphene (tBLG) has recently fueled a renewed interest in a special subset of such heterostructures, namely twisted bi- and multilayer structures [6–12]. The experimental observations now range from correlated insulator phases [13] intercepted with magic angle superconductivity in twisted bilayer graphene [5,7,14–26], superconductivity in twisted trilayer graphene [27,28] to highly correlated states [19,29–35] and (anti)ferromagnetic signatures [32,36–40]. However, experimental devices may include twist angle disorder and relative displacements between the layers, as well as anharmonicities, that manifest themselves also in the phonon properties [41] complicating the observation of such effects. In tBLG at angles close to the magic angle, theory predicts perfectly flat bands [1,42] induced by interlayer hybridization, with correlation effects leading to multiple topological transitions [43,44]. Flat bands are also seen as the main driving mechanisms for moiré-induced superconductivity [29]. Nevertheless, understanding the precise nature of the observed effects is still an ongoing debate [45–47].

Beyond the modification of the electronic structure, the moiré-induced superlattice also modifies the phononic dispersion relation [9,48–52]. These modifications are much more subtle, yet in particular the low-energy shear and breathing modes [52] might be critical in the understanding of some correlated phenomena. Given the critical role of electron-phonon coupling for understanding conventional BCS-like superconductors, a quantitative understanding of the moiré-induced changes seems key in unraveling the exotic superconducting state of tBLG.

Efforts to capture the experimental observations regarding the electronic structure numerically have been significant and reach from effective many-body Hamiltonians such as the Hubbard model [53] or Fermi-liquid theory [54], Hatree-Fock diagonalization schemes [55] to single-particle supercell models [56,57]. One particularly successful method, initially introduced by Bistritzer *et al.* [1] models the interaction between the low-energy bands in momentum space using a single-particle continuum model. Such a description allows for studying the continuous evolution of the electronic structure and related physical properties with twist angle, without the need to resort to large real-space supercells. In the tBLG case one single parameter describes the effect introduced by the moiré periodicity. This formalism has meanwhile been applied to the electronic band structure of a number of other heterostructures [58,59]. We have recently derived a similar model to describe the evolution of the phonon band structure in transition metal dichalcogenides [52]: the moiré couples low-energy acoustic modes and layer-breathing modes (LBM), strongly modifying the phonon band structure at low twist angles. In the present paper we extend our model to more accurately include subtle long-range interactions induced by the moiré. We investigate the moiré-induced coupling of phonon branches in twisted bilayer graphene as a function of twist angle and identify a series of avoided crossings that strongly modify the phonon band structure and thus the phonon density of states at low twist angles.

The low-energy phonon modes in tBLG have already been investigated through several models in the literature [9,48–51]. In-plane asymmetric acoustic phonon modes were found to form minibands separated by gaps [48]. When dealing with very small twist angles, these modes can be related

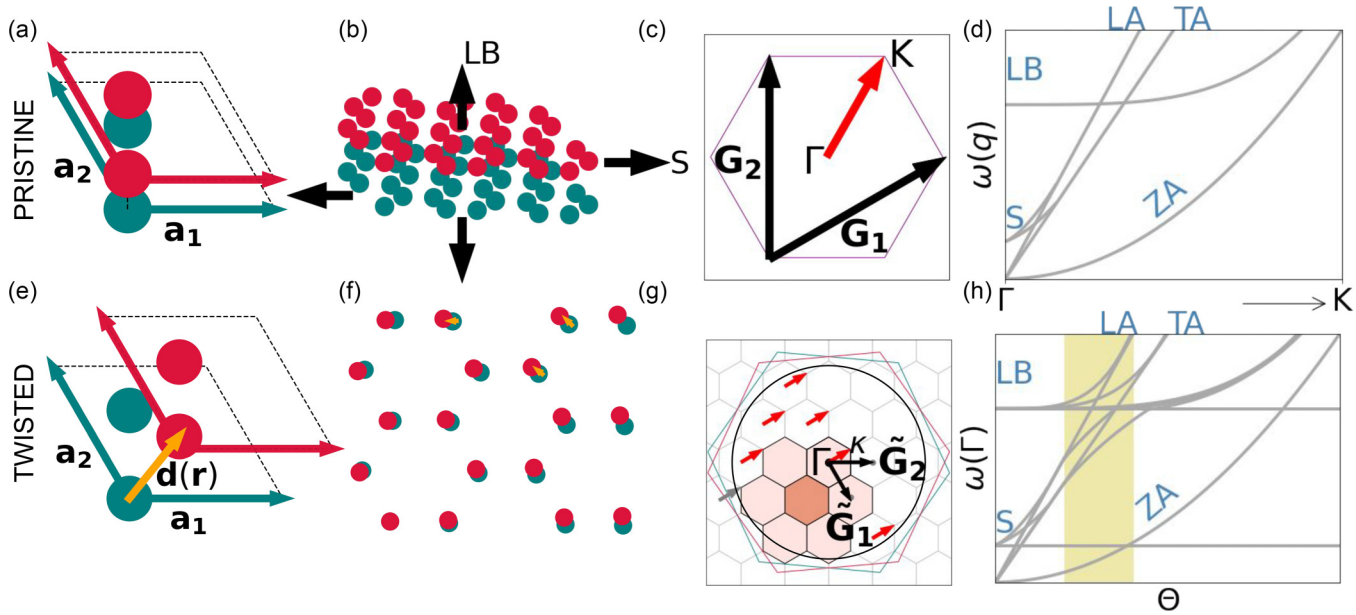

FIG. 1. Comparison of pristine BLG (top row) and twisted BLG (bottom row). (a) Pristine bilayer unit cell. (b) Schematic representation of the two new modes appearing in bilayer systems: the layer breathing (LB) mode and the shear mode (S). (c) Pristine BLG Brillouin zone, spanned by reciprocal lattice vectors $\mathbf{G_1}$ and $\mathbf{G_2}$. A red arrow denotes the path from Γ to K. (d) Schematic of the phonon band structure of BLG plotted along the first third of the red arrow from panel (c). [(e), (f)] For a moiré supercell at small twist angles, we can neglect the local rotation between atoms in the top and bottom layer. Then, there is only a local displacement $\mathbf{d}(\mathbf{r})$ between the atoms in the top and bottom layer that varies within the supercell. (g) Relation of reciprocal representations of pristine and twisted BLG: twisted Brillouin zones of the top and bottom layer (large red and blue hexagons), as well as moiré Brillouin zones (grey) rotated by 90° with respect to the pristine cells. Lightly shaded red hexagons exemplify the coupling between the first shell of neighboring Γ points. The small red arrows connecting moiré Γ to K explain the concept of phonon backfolding (see main text). (h) Schematic evolution of the phonon bands at Γ with twist angle. Note the similarity to (d) due to phonon backfolding. The LB and TA/LA feature a pronounced avoided crossing (shaded yellow area) induced by the coupling to neighboring moiré Γ points [see (g)].

to the oscillation of the domain wall boundaries between commensurate AB sites. These modes were referred to as phason modes [9,49]. From a group-theoretical perspective, these moiré phonon modes and the underlying gaps emerge from an additional mismatch symmetry related to the in-plane translation of one lattice with respect to the other, reconciling these two seemingly different viewpoints in the small angle limit [50]. Conversely, our model operates in momentum space, and is thus not limited to a discrete set of commensurate angles. This allows calculating the continuous evolution of the phonon density of states with twist angle, irrespective of whether the underlying supercell is commensurate or not. We can thus focus on the evolution of the avoided crossing between acoustic and breathing modes. We identify band gaps formed in the phonon band structure, in line with the gaps found in the literature [48,50]. In particular, an avoided crossing emerges at the twist angle where the LBM becomes degenerate with the backfolded acoustic branch at Γ. Relaxation of the bilayer system and the associated change in the supercell geometry strongly affect the phonon coupling. In particular around 2°, the LBM broadens considerably due to the different interlayer spacings within one moiré cell [60].

Our findings are applicable to (homo)bilayers beyond bilayer graphene: The acoustic and layer-breathing modes will—for most values of the interlayer coupling and the in-plane speed of sound—feature a crossing. The moiré induces an interaction between these two modes, strongly modifying the phonon band structure at the crossing, thus opening a further playing field towards designed material properties.

This paper is organized as follows: We first present our model for the phonon band structure of homobilayer systems including strain in Sec. II. We then apply our model to twisted bilayer graphene (Sec. III), and discuss the impact of the moiré on the phonon density of states as a function of twist angle. We conclude with a discussion of the applicability of our results to the general case of homobilayers. We provide a comprehensive definition of the moiré dynamical matrix in Appendix A, and briefly discuss the role of the cutoff in reciprocal space in Appendix B, and of strain in Appendix C.

II. MODEL

A pristine honeycomb lattice is defined by the two unit vectors $\mathbf{a}_1 = a(1, 0)$ and $\mathbf{a}_2 = \frac{a}{2}(-1, \sqrt{3})$, which in turn determine the reciprocal cell vectors $\mathbf{G}_{1,2}$ via $\mathbf{a}_i \cdot \mathbf{G}_j = 2\pi\delta_{ij}$. Aligning two lattices on top of each other [see Fig. 1(a)] does not affect the in-plane periodicity in the unit cell, creating a pristine bilayer with a hexagonal Brillouin zone [Fig. 1(c)] spanned by $\mathbf{G}_1 = \frac{2\pi}{\sqrt{3}a}(\sqrt{3}, 1)$ and $\mathbf{G}_2 = \frac{4\pi}{\sqrt{3}a}(0, 1)$. When considering the phonons of this bilayer as compared to the individual monolayers, two obvious new modes emerge [Fig. 1(b)]: the layer-breathing mode (LB), where the interlayer spacing oscillates, and the (two) shear modes (S), corresponding to a relative in-plane motion of the two layers.

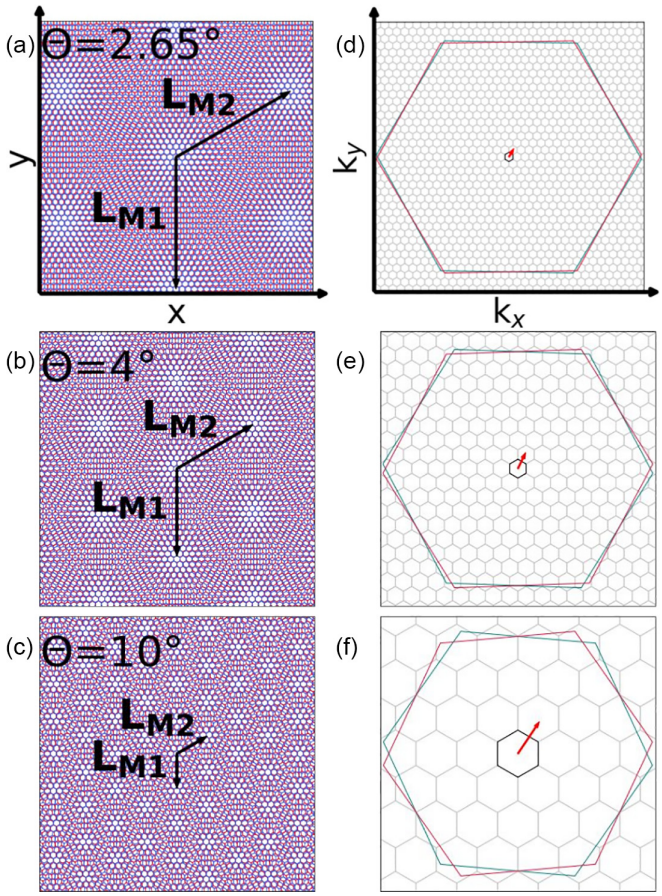

FIG. 2. Real space (left column) and reciprocal space (right column) representation of a twisted honeycomb bilayer for various twist angles. As the real-space unit-cell size decreases, the reciprocal unit-cell size increases. The red arrow in the second column demonstrates how the distance between the neighboring $\tilde{\mathbf{G}}$ points expands for larger twist angles. The first row refers to the magic twist angle (2.65°) for which the moiré BZs perfectly fit inside the pristine one. The other two rows refer to nonmagical angles (4° and 10°).

In general, the low-energy phonon band structure of such a bilayer will thus, to first order, feature the acoustic modes of the monolayers (LA, TA, and the parabolic ZA typical for two-dimensional crystals) as well as the shear and breathing modes [Fig. 1(d)]. At a specific q value the breathing mode LB (determined by the interlayer coupling) and the linear acoustic branches, LA and TA, will cross. In homobilayers where each layer features at least σ_h symmetry, this crossing is protected by symmetry (different parity with respect to the out-of-plane coordinate z).

Combining two such lattices with a relative twist angle Θ creates a moiré superstructure, forming a large quasi-supercell in real space [61], with a correspondingly small reciprocal one (Fig. 2). The moiré lattice vectors in the small twist angle limit are connected via $\mathbf{L_{M1,M2}} = -\frac{1}{\Theta}\hat{z} \times \mathbf{a_{1,2}}$. Reciprocal lattice vectors for the twisted bilayer system can be similarly obtained as $\tilde{\mathbf{G}}_{\mathbf{1,2}} \approx -\Theta\hat{z} \times \mathbf{G_{1,2}}$. Generally, an arbitrary twist angle will not yield a commensurate unit cell and, consequently, Bloch's theorem does not necessarily apply. This inconvenience greatly complicates the theoretical modeling of the electronic structure [1,47]. Using a continuum model in reciprocal space [1] allows treatment of incommensurate bilayer structures. It can be used to calculate a low-energy electronic band structure of twisted bilayers by introducing a weakly position-dependent interlayer hopping to the low-energy Dirac electrons in each layer. The Hamiltonian is periodic with the moiré period, and instead of Bloch bands, one can theoretically approach the system by using moiré bands. This model was extended and adjusted for *ab initio* electronic structure calculations by Jung *et al.* [59]. The same framework, however, can be transferred to the phononic system with some changes [52].

A finite twist angle changes the local electronic environment of each atom. For small twist angles, the local rotation between unit cells in the top and bottom layers can be neglected in favor of only considering a rigid displacement vector $\mathbf{d}(\mathbf{r})$ between the unrotated top and bottom layer [see Figs. 1(e) and 1(f)]. In the small angle approximation, $\mathbf{d}(\mathbf{r})$ can then be explicitly written as

$$\mathbf{d}(\mathbf{r}) \approx -\Theta\hat{z} \times \mathbf{r}, \tag{1}$$

while the reciprocal vector $\mathbf{G}$ rotates into $\tilde{\mathbf{G}}(\Theta, \mathbf{G}) \approx -\Theta\hat{z} \times \mathbf{G}$. All displacements $\mathbf{d}(\mathbf{r})$ lie within the unit cell of the pristine lattice. Consequently, one can map each local configuration at a point $\mathbf{r}$ of the moiré supercell to a rigid displacement $\mathbf{d}(\mathbf{r})$ in so-called configuration space mapped on the unit cell of the pristine lattice.

We aim to calculate the phonon band structure of the moiré superstructure. Phonon eigenmodes ω are typically calculated as the eigenvectors (and associated eigenfrequencies) of the dynamical matrix $\overline{\mathrm{D}}$ of the crystal,

$$D(\mathbf{q})_{j,j'} = \frac{1}{\sqrt{M_j M'_j}} \sum_{\mathbf{R}-\mathbf{R}'} e^{i\mathbf{q}\mathbf{R}} C_{j,j'}(\mathbf{R}-\mathbf{R}') e^{-i\mathbf{q}\mathbf{R}'}, \tag{2}$$

with indices j, j', running over the $3N$ degrees of freedom of the moiré unit cell. The entries of $\overline{D}$ are the Fourier transforms of the Hessians C containing the interatomic force constants, typically obtained from density functional perturbation theory [62–64]. We focus on the regime of small twist angles, when the pristine unit cell is much smaller than the moiré supercell. Unfortunately, exactly calculating the $3N \times 3N$ matrix of force constants for a supermoiré with $N \gg 5000$ atoms quickly becomes unfeasible. The key insight is that for a given twist angle, there is a continuous, bijective mapping between the index of an atom j in the moiré supercell, its position in the unit cell $\mathbf{R}_j$, and the local stacking $\mathbf{d}$ at that point in the cell. Strain and the resulting distortion may locally warp this map as discussed below, yet it will remain continuous and bijective. Based on $\mathbf{d}(j)$ we can rewrite the force constants in Eq. (2) as

$$C_{j,j'} = \frac{\partial^2 V}{\partial r_j \partial r_{j'}} \rightarrow C_{\alpha,\alpha'}(\mathbf{R}-\mathbf{R}'|\mathbf{d}), \tag{3}$$

with indices α, α' running over the degrees of freedom in one pristine bilayer unit cell only, and an explicit dependence on the position within the moiré. Rotating a linear combination of the large moiré unit cell vectors via $\Theta\hat{z} \times \mathbf{L_M}$ gives a linear combination of the pristine unit-cell vectors $\mathbf{a}_i$. Combined with Eq. (1) this leads to the expression $\mathbf{d}(\mathbf{r} + \mathbf{L_M}) =$

$\mathbf{d}(\mathbf{r}) + \mathbf{a}$, confirming that $\mathbf{d}(\mathbf{r})$ is periodic with moiré periodicity $\mathbf{L}_M$ and maps onto the pristine unit cell with periodicity $\mathbf{a}$. Furthermore, we assume $\mathbf{d}(\mathbf{r})$ is sufficiently smooth over the area of one pristine unit cell denoted by subscript p to approximate $\mathbf{d}(\mathbf{r}) \approx \mathbf{d}(\mathbf{R_p})$. This assumption is valid for small twist angles, when the pristine unit cell is much smaller than the moiré supercell. The variation of the force constants with $\mathbf{d}$ can therefore be expanded in terms of pristine reciprocal lattice vectors $\mathbf{G}$,

$$C_{\alpha,\alpha'}(\mathbf{R}''|\mathbf{d}) = \sum_{\mathbf{G}} C_{\alpha,\alpha'}(\mathbf{R}''|\mathbf{G}) e^{-i\mathbf{d}\mathbf{G}}. \tag{4}$$

This Fourier transformation can be considered as a perturbative expansion. Given the much smaller Brillouin zone of the twisted superstructure, the phonon dispersion of the pristine bilayer [e.g., along the red arrow in Fig. 1(c)] is backfolded at the new Brillouin zone edges. The lowest-order contribution (i.e., the zeroth-order Fourier component) is given by the average of the force constants over all stackings. The resulting phonon band structure would consist of the backfolded phonon branches of twisted bilayer graphene. The higher Fourier components in Eq. (4) describe the spatial variations of the atomic stacking induced by the moiré, due to the variations in the respective force constants within the moiré supercell. As a result, small but important couplings between the backfolded branches emerge. Here we extend our framework to more accurately treat these moiré-induced interactions between backfolded phonon branches. We calculate the phonon band structure of tBLG and evaluate several derived quantities to elucidate the effect of the moiré on structural properties. For a full derivation and technical details, see Appendix A.

To obtain the Fourier expansion required in Eq. (4), we sample configuration space using a 10×10 grid. For each of these one hundred $\mathbf{d}$ values, we perform a density functional perturbation theory (DFPT) calculation [64]. Note that each calculation only involves four atoms in the bilayer unit cell except the explicitly $\mathbf{q}$-dependent intralayer contributions which require a 5×5 cell. We can thus parametrize the local electronic structure of the much larger moiré supercell, including the energy $V(\mathbf{d})$ of the local alignment $\mathbf{d}$. For each local alignment $\mathbf{d}$, we fix the relative positions of the atoms in the bilayer plane, and relax the layer spacing. In the absence of strain, the geometrical mapping from a position $\mathbf{r}$ in the supercell to $\mathbf{d}(\mathbf{r})$ of Eq. (1) is sufficiently smooth to warrant this approximation. The assembly of $\overline{D}(\mathbf{q})$ using the Fourier-transformed force constants obtained from individual (cheap) DFT calculations of the bilayer unit cell then represents an efficient yet highly accurate approach. Note that most of these individual calculations do not correspond to a fully relaxed geometry (as $\mathbf{d}$ is fixed), and thus do not represent physical Hessians. Indeed, the individual calculations only serve to provide parameters for approximating the force constants in Eq. (4), and thus ultimately the dynamical matrix in Eq. (2), which is physical. Since the coupling elements vary smoothly as a function of position within the moiré, an obvious strategy to reduce the problem size is to truncate the Fourier expansion in Eq. (4), substantially reducing the problem size. Before discussing the approximations and validity of such a truncation,

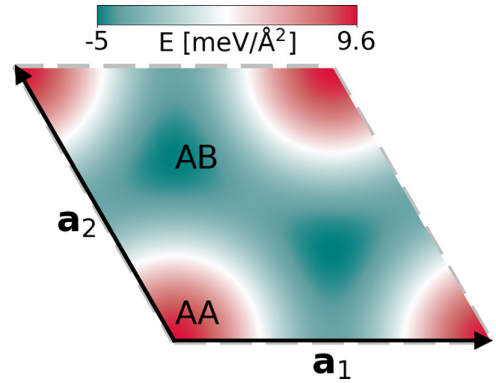

FIG. 3. Generalized stacking fault energy in configuration space. The pristine unit cell size indicates the scale. AA and AB indications highlight typical stacking configuration in the corresponding real space picture.

we include strain and the resulting relaxation of the lattice, as described in the following paragraphs.

Each local $\mathbf{d}$ corresponds to a specific local (mis)alignment, and an associated stacking energy. Assuming no lattice relaxation, the mapping $\mathbf{d}(\mathbf{r})$ is simply given by Eq. (1). However, the large size of the moiré unit cell for small-angle tBLG allows the lattice to relax by enlarging energetically favorable stacking areas. At very small angles $\Theta < 2^\circ$, the resulting geometric relaxation of the moiré pattern leads to extended regions of energetically favorable AB stacking separated by domain walls. This reconstruction has already been experimentally observed [65–67] and numerically parameterized [9,51,52,57,68–70], proving that twisted structures are not a simple rigid shift of the atoms. By contrast, at large twist angles $\Theta > 10^\circ$, the moiré superstructure becomes too small to allow for meaningful relaxations. Modeling the relaxation between these two limiting cases is critical to correctly capture the electronic and phononic properties of the lattice. We use a continuum elasticity model first suggested by Nam *et al.* [57] to calculate the effects of lattice reconstruction in tBLG. In this picture, the relaxation is described as a distortion of the simple geometrical mapping of Eq. (1). We denote by $\mathbf{u_t}$ and $\mathbf{u_b}$ the absolute local displacements of the top and bottom layer from the rigid honeycomb lattice, and then

$$\mathbf{d}(\mathbf{r}) \to \mathbf{d}(\mathbf{r}) + \mathbf{u}_t(\mathbf{r}) - \mathbf{u}_b(\mathbf{r}). \tag{5}$$

$\mathrm{U_B}$ describes the interaction between layers as an effective generalized stacking fault energy (GSFE), see Fig. 3. Integrating the potential profile over space yields the total interlayer binding energy

$$\mathrm{U_B}[\mathbf{u}_t, \mathbf{u}_b] = \int V[\mathbf{u}_t(r) - \mathbf{u}_b(r)] d^2\mathbf{r}. \tag{6}$$

The potential profile depends on the local stacking configurations. We therefore calculate it in configuration space as a function of the displacement vector $\mathbf{d}$. As it is periodic within the pristine unit cell the simplest option for its functional dependence is $V[\mathbf{u_t}, \mathbf{u_b}] = \sum_G c_\mathbf{G} \cos((\mathbf{u_t}(\mathbf{r}) - \mathbf{u_b}(\mathbf{r}) + \mathbf{d}(\mathbf{r})) \cdot$

G). The elastic energy is defined as [57]

$$\mathrm{U}_E = \sum_{l=1}^{2} \int \frac{1}{2}\Big\{(\lambda+\mu)\big(u_{xx}^{(l)}+u_{yy}^{(l)}\big)^2 + \mu\Big[\big(u_{xx}^{(l)}-u_{yy}^{(l)}\big)^2 + 4\big(u_{xy}^{(l)}\big)^2\Big]\Big\} d^2\mathbf{r} \tag{7}$$

with the typical values of graphene's Lamé factors $\lambda \approx 3.5\mathrm{eV/\AA^2}$ and $\mu \approx 7.8\mathrm{eV/\AA^2}$, which characterize the stiffness of the lattice. Reducing the interlayer binding energy ($\mathrm{U_B}$) involves straining the membrane and thus increasing the intralayer elastic energy ($\mathrm{U_E}$). The competition between these two contributions results in a minimized total potential energy functional with respect to the relative displacement between the two layers forming an Euler-Lagrange set of equations. The energy functional can be written as

$$\mathrm{U_{tot}} = \mathrm{U_B}[\mathbf{u}^t, \mathbf{u}^b] + \mathrm{U_E}[\mathbf{u}^t] + \mathrm{U_E}[\mathbf{u}^b]. \tag{8}$$

Minimization of $\mathrm{U_{tot}}$ typically decreases the size of AA stacked regions, and reduces the symmetry of the superstructure (see Fig. 9).

After determining the geometry of the relaxed supercell, we proceed with calculating the phonon band structure based on Eq. (2). Due to the spatial dependence of **d** of the force constants in Eq. (3), these matrices become non-diagonal in reciprocal space within the given model. We assemble the moiré dynamical matrix as a Fourier sum of the force constants for all configurations,

$$D^m_{\alpha,\alpha'}(\mathbf{q},\mathbf{q}') = \frac{1}{\sqrt{M_\alpha M_{\alpha'}}} \cdot \sum_{\mathbf{R},\mathbf{R}'} \sum_{\mathbf{G}} C_{\alpha,\alpha'}(\mathbf{R}'|\mathbf{G}) \times e^{i\mathbf{q}'\mathbf{R}'} e^{i(\mathbf{q}-\mathbf{q}'-\tilde{\mathbf{G}})\mathbf{R}}, \tag{9}$$

where the matrix form is indicated with a bar. Since $\mathbf{u}^t$ and $\mathbf{u}^b$ both depend on the twist angle Θ when considering relaxation effects, the angle dependence enters the dynamical matrix through the displacement vector $\mathbf{d}(\mathbf{r})$. From Eq. (5) it follows that

$$\overline{\mathrm{D}}(\mathbf{q}' \mid \mathbf{d}) \to \overline{\mathrm{D}}(\mathbf{q}' \mid \mathbf{d} + \mathbf{u}_t - \mathbf{u}_b) \to \overline{\mathrm{D}}(\mathbf{q}'|\mathbf{d}, \Theta), \tag{10}$$

where we have dropped writing the $\mathbf{r}$ dependence of $\mathbf{d}$, $\mathbf{u}_t$, and $\mathbf{u}_b$ for brevity. For each twist angle Θ, instead of a rigid $\mathbf{d}$ shift, we use Eq. (5) to obtain $\overline{\mathrm{D}}(\mathbf{q}' \mid \mathbf{d}, \Theta)$ and perform its Fourier transform for each angle independently. For calculating only the frequencies close to the central $\mathbf{\Gamma}$ point, further approximations can be made. We separate the sum Eq. (9) in two terms, $\mathbf{G} = 0$ and $\mathbf{G} \neq 0$, and only keep the $\mathbf{q}$ dependence in the diagonal terms ($\mathbf{G} = 0$) of the moire dynamical matrix. In the small-angle approximation ($|\tilde{\mathbf{G}}| \ll |\mathbf{G}|$) we can reduce $\overline{\mathrm{D}}(\mathbf{q}' \mid \mathbf{G} \neq \mathbf{0})$ to $\overline{\mathrm{D}}(\mathbf{\Gamma} \mid \mathbf{G} \neq 0)$. Furthermore, since $|\overline{\mathrm{D}}(\mathbf{q} \mid \mathbf{G})|$ quickly approaches zero as $|\mathbf{G}|$ increases we truncate the reciprocal expansion after just a few unit vectors. In the simplest model [52] this would mean truncating the expansion to the six nearest neighbours, leaving us with the moiré dynamical matrix

$$\overline{\mathrm{D}}^m(\mathbf{q}) \approx \begin{pmatrix} \overline{\mathrm{D}}(\mathbf{q} \mid \mathbf{0}) & \overline{\mathrm{D}}(\mathbf{\Gamma} \mid \mathbf{G}_1) & \overline{\mathrm{D}}(\mathbf{\Gamma} \mid \mathbf{G}_2) & \cdots & \overline{\mathrm{D}}(\mathbf{\Gamma} \mid \mathbf{G}_6) \\ \overline{\mathrm{D}}^\dagger(\mathbf{\Gamma} \mid \mathbf{G}_1) & \overline{\mathrm{D}}\big(\mathbf{q}+\tilde{\mathbf{G}}_1 \mid \mathbf{0}\big) & & & \\ \overline{\mathrm{D}}^\dagger(\mathbf{\Gamma} \mid \mathbf{G}_2) & & \overline{\mathrm{D}}\big(\mathbf{q}+\tilde{\mathbf{G}}_2 \mid \mathbf{0}\big) & & \\ \vdots & & & \ddots & \\ \overline{\mathrm{D}}^\dagger(\mathbf{\Gamma} \mid \mathbf{G}_6) & & & & \overline{\mathrm{D}}\big(\mathbf{q}+\tilde{\mathbf{G}}_6 \mid \mathbf{0}\big) \end{pmatrix}. \tag{11}$$

An alternative way to understand the additional matrix dimensions of Eq. (11) is to consider a basis change of the full dynamical matrix of the moiré superstructure from real space to Fourier space (see Appendix A 2). Such a unitary transformation leaves the eigenvalues invariant. Restricting the matrix dimensions to, e.g., the six neighboring Γ points as in Eq. (11) then corresponds to truncating the Fourier basis, since the matrix elements for larger **G** vectors quickly decay. The number of **G** vectors to consider obviously depends on the size of the moiré supercell, i.e., on the twist angle. At small twist angles, a larger number of moiré backfolded phonon branches (i.e., a larger number of Fourier basis elements) should be considered using a similar energetic cutoff. For this reason, a small twist angle moiré dynamical matrix includes a larger number of moiré $\tilde{\mathbf{\Gamma}}$ points (see Fig. 2) and thus features a larger dimension, depending on the number of moiré BZs contained inside the large pristine one [denoted by a circle in Fig. 1(g)]. The off-diagonal elements in the moiré dynamical matrix are responsible for coupling one specific $\tilde{\mathbf{G}}$ point to the first shell of its neighboring ones [red shaded hexagons in Fig. 1(g)] and therefore, also for degeneracy lifting (see Appendix A 2). Indeed, considering too few interactions in momentum space results in unphysical discontinuities in the phonon band structure (see Appendix B). To avoid such artefacts, we increase the cutoff radius with decreasing twist angle, carefully ensuring to obtain a converged phonon band structure. As we have verified numerically, our phonon band structures are converged with respect to the number of included $\tilde{\mathbf{G}}$ points—or, put differently, with respect to the number of Fourier components considered in the expansion of Eq. (4). While we focus on phonons in the present paper, we note that a similar model could be applied in the derivation of electron-phonon matrix elements for a continuous range of twist angles.

III. APPLICATION

Having established the low-energy continuum model for phonons in homobilayers we now apply the model to twisted

bilayer graphene. Only considering the interaction between the original Γ point and its six nearest neighbors [i.e., Eq. (11)] for tBLG produces a band structure of $(6+1)\times 12 = 84$ phonons due to the twelve branches backfolded in the moiré Brillouin zone at the Γ point and its six neighbors. Small twist angles require a correspondingly larger (outer) cutoff since even more backfolding occurs, resulting in an overall larger dynamical matrix dimension (for details see Appendix A).

Similar to the pristine case, the usual transverse and longitudinal acoustic modes dominate the low-energy phonon spectra [see schematic in Fig. 1(d)]. Longitudinal, transverse, and out-of-plane acoustic (optical) modes are denoted as usual by LA(O), TA(O), and ZA(O). However, in bilayers two types of new modes emerge: the shear (breathing) modes involve parallel (perpendicular) relative motion of the two layers [see Fig. 1(b)].

Beyond these special bilayer modes, the effect of a finite twist angle is twofold: (i) the large real-space supercell results in several phonon branches and (ii) the coupling mediated by the moiré potential lifts the degeneracy between these branches and couples the acoustic and breathing modes [compare grey and blue lines in Fig. 4]. The strong **d** dependence of the moiré dynamical matrix is responsible for the finite coupling between these modes. The induced avoided crossings are a major effect of the moiré potential, and can serve as a measure of strength of the variation in coupling. We first discuss the evolution of the LBM frequency with twist angle. At very small twist angles, the energetically favorable AB stacking dominates the breathing mode frequency. Note that neglecting relaxation will lead to a quite broad LBM peak already at $\Theta \to 0$ (see red lines in Fig. 4). Conversely, accounting for too few interactions within the moiré dynamical matrix (i.e., a too low cutoff) strongly underestimates the spread of these avoided crossings (see Appendix B for a more detailed comparison). Once the two acoustic modes cross with the LBM at 1° and 2° degrees, (see arrows in Fig. 4), a complicated peak structure emerges in the phonon density of states (see rightmost panels in Fig. 4). While smaller Raman shifts for the breathing modes are more challenging to measure, good setups can provide resolutions of the order of a few cm^{-1} for the breathing modes, as, e.g., in the angle-resolved evolution of the breathing mode frequency for MoS_2 [52]. The modulations in breathing mode width and frequency should thus be well visible in Raman measurements of the LBM at these small twist angles. Note that such a broad Raman peak could also be (miss)interpreted as due to inhomogeneities in the sample, which is obviously not the case for our model. High but realistic experimental resolution should be able to resolve the substructure at $\Theta \approx 3-6°$. At even larger twist angles, the interlayer spacing increases as the coupling between the twisted layers is reduced, which strongly reduces the spread of its peak in the phonon density of states (PDOS).

We focus next on the evolution of the shear mode with the twist angle. For zero coupling, the shear mode at the central Γ point resides at a frequency of $10\,\mathrm{cm}^{-1}$ (see Fig. 4), featuring only a weak angle dependence. At very low twist angles, relaxation of the moiré lattice leads to the appearance of phasons related to vibrations of the boundaries between AB regions [9,49]. At such boundaries, the local stackings

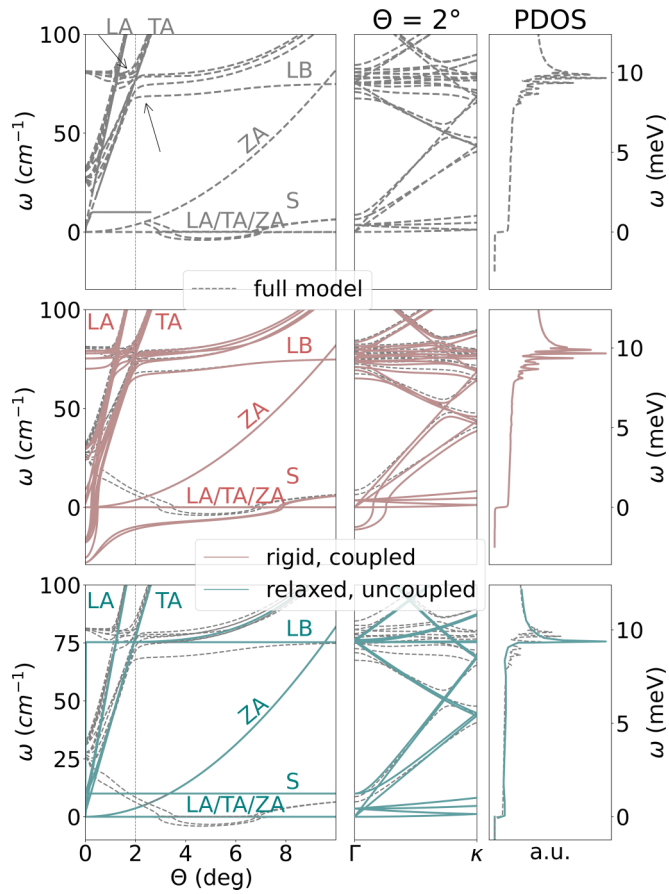

FIG. 4. Twist angle dependent evolution of phonon modes. Left panel: Evaluated at the central Γ point as a function of twist angle. Central panel: Evaluated along the path $\Gamma \to K$ at twist angle 2°. Right panel: Density of states at twist angle 2°. The contributions of individual parts of the model can be clearly assigned. When the Γ off-diagonal contributions are neglected (cyan lines) no coupling between individual modes is observed, when relaxation is neglected (red lines) imaginary frequencies emerge at small twist angles, causing an unstable lattice. Only including both contributions (dashed lines) resembles a realistic phonon dispersion scenario.

change rapidly, and the membrane is not able to relax to the respective equilibrium distances for each stacking. In this context, we need to reevaluate the approximations involved in evaluating the force constants of Eq. (4) in light of the remapping in Eq. (10). At the boundaries between AB regions, the stacking changes rapidly over a relatively short distance—consequently, the lattice cannot relax to the corresponding layer spacing at each stacking. In our formalism, we evaluate the different dynamical matrices at fixed distances for each **d**, choosing the equilibrium spacings for each stacking. Consequently, the dynamical matrices we calculate are taken at the wrong layer spacing—leading to a poor description of these phason modes by our approach (see also Appendix D). For the same reason, we also observe negative phonon frequencies at intermediate twist angles between 4° and 7°. Lattice relaxation at small twist angles offsets this effect as the lattice corrugation allows for relaxation to the respective equilibrium distances at the high-symmetry points of the moiré. Indeed, neglecting the corrugation entirely leads to much larger imagi-

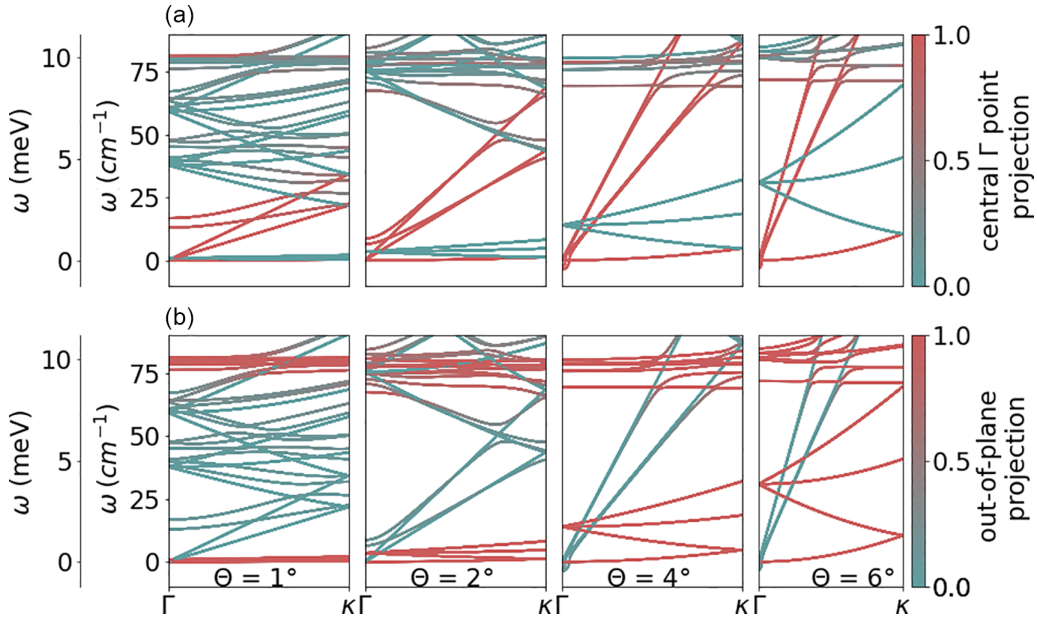

FIG. 5. Projected phonon bandstructure on (a) the central Γ point and (b) on the out-of-plane component of the eigenvectors.

nary contributions also at small angles (see red lines in Fig. 4). At large twist angles $\Theta > 8°$, relaxation no longer plays a role (i.e., red and grey lines coincide for $\Theta > 8°$ in Fig. 4). For intermediate twist angles $4° < \Theta < 7°$ as well as phason modes, however, our model underestimates the shear mode frequency. For those angles the interlayer spacing is smaller than what we assume due to the mechanical constraints imposed by the lattice geometry. Given the comparatively weak dependence of the force constants with layer spacing in van der Waals bondings, we do not expect this approximation to be problematic at high energies, where the phonon band structure is dominated by the high-energy vibrations of the covalent bonds within each lattice. The backfolding effect depends on the size of the moiré BZ, or the twist angle (see Fig. 5). The slope of the shear mode appears steeper as the angle increases due to the increase of the distance between Γ and K (see Fig. 2). As a consequence, the ZA branches backfold at lower frequencies for smaller twist angle, producing an indistinguishable multitude of modes at, e.g., $\Theta = 1°$. For very small twist angles, the LA and TA modes backfold, and the breathing mode eventually disappears among them. A pronounced avoided crossing emerges for $\Theta > 3°$. Generally, the expected angle Θ for an avoided crossing can be calculated if the LBM frequency and the slopes of the acoustic branches are known for the system in question, leading to the qualitative picture shown in Fig. 1(h). As for the shear mode, due to its steep slope, its contribution to the PDOS will be quite small. By projecting the phonon dispersion on the out-of-plane axis or on the central Γ point (see Fig. 5), one can distinguish, i.e., which acoustic branches originate at the central Γ as well as which breathing mode branch. The flat modes at the frequency of $80\,\mathrm{cm}^{-1}$ correspond to the modes originating entirely at neighboring Γ points. In the out-of-plane projection, one can easily distinguish the two contributions, namely the flat breathing mode and the ZA phonon mode. Both of them strongly contribute to the total PDOS, leaving it almost unaltered after projecting on the out-of-plane axis. For small twist angles, the missing contribution from the total PDOS will thus be the one from LA and TA backfolded branches. The projected phonon dispersions can be calculated by weighting the frequencies with the corresponding norm of the eigenvectors distributed over the central BZ for the central Γ-point projection, or belonging to their z component for the out-of-plane projection. To elucidate the changes in the dispersion with twist angle, we calculate the evolution of the PDOS with the twist angle (see Fig. 6). The dominant contribution corresponds to the flat and only weakly angle-dependent breathing mode at $75\,\mathrm{cm}^{-1}$. The experimentally observed breathing mode frequency value of $94\,\mathrm{cm}^{-1}$ [71] is not obtained here, due to the use of LDA functionals. While overestimating the binding energy, LDA functional underestimates the phonon energies. As the twist angle increases, one branch of the breathing mode disappears merging with the acoustic modes, while another one emerges—the two form an avoided crossing. The second peak at larger twist angles derives from the modes originating at neighboring moiré Γ points. At very small twist angles the system may relax considerably, leading to an intricate structure. The stability of such a relaxed supercell influences the phonons in the system and the main differences lie in the small frequency range around $80\,\mathrm{cm}^{-1}$. In the relaxed case, there is a sharp maximum at $81\,\mathrm{cm}^{-1}$ because the lowest-energy AB stacking and its associated LBM frequency dominate the supercell geometry. A stripe-like pattern continues for larger twist angles, where the lattice enters the rigid regime with very weak coupling between the two layers. The weak twist-angle dependence in this regime is expected from the reduced size of the supermoiré unit cell, smaller corrugation and weaker interlayer interactions [52,72]. This is also the reason why we can employ the small twist angle approximation for angles up to 10°: the influence of the moiré at these angles is small anyway. In the rigid case, a much broader feature around the main contribution appears. The same feature is visible in Fig. 4, with merged and dispersed modes in the relaxed and rigid case

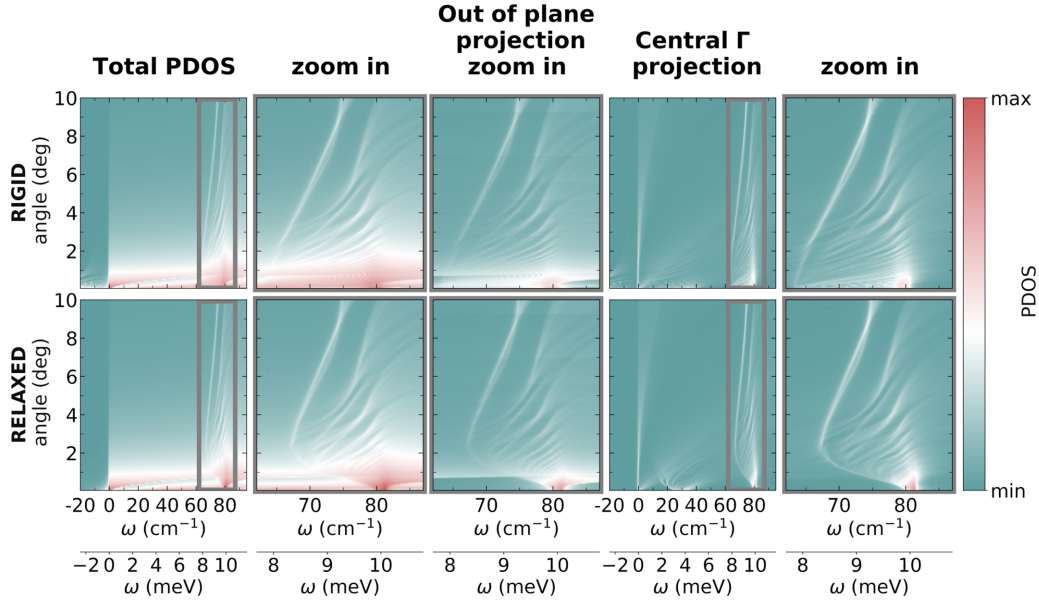

FIG. 6. Phonon density of states. The first two columns show the phonon density of states in the rigid and relaxed regime. The third column represents an out-of-plane projection of the eigenmodes, while the last two columns show a central Γ point projection. A discontinuous transition between $\Theta < 1^\circ$ and $\Theta > 1^\circ$ is the effect of the energetic cutoff used in the calculation. For very small angles, a large number of small BZs should be included in the calculation, but due to numerical feasibility, the largest outer cutoff (see Fig. B in Appendix) we use is 12. In other words, as the angle decreases, the outer cutoff is increasing, but we limit its maximum value to 12, which becomes insufficient and we see a discontinuity in the PDOS. At small twist angles, the modes are "pushed" to smaller energies, making the contributions at larger energies inaccessible in the calculation if additional BZs are not included in the calculation.

respectively. However, it is not the relaxation that broadens the LB mode, but the off-diagonal moiré dynamical matrix elements. The overall "stripe-like" appearance of the PDOS is a direct consequence of the low-energy band structure in Fig. 5. As the angle decreases, the majority of the backfolding occurs at lower frequencies, leading to the appearance of a larger number of flat modes contributing significantly to the density of states and creating a set of displaced maxima.

We finally discuss projections of the phonon eigenmodes on the out-of-plane components of the eigenvectors and the central Γ. By projecting the phonon modes on the out-of-plane component of the eigenvectors, one can identify which modes feature out-of-plane movement of the atoms. The breathing mode represents the motion of the two graphene sheets perpendicular to their plane of propagation and therefore has the largest contribution to the corresponding projected density of states. At low twist angles, the corresponding PDOS features a reduced contribution below $80\,\mathrm{cm}^{-1}$, due to missing in plane acoustic modes in the out-of-plane projection. These features are well highlighted by the color-coded out-of-plane projection in Fig. 5(b). The projected phonon density of states on the central Γ point reveals the modes, which originate in the central Γ point and serves as an approximation of the optical activity in, e.g., Raman measurements. The peak at low frequencies corresponds to the optically active shear mode, which at small twist angles $\Theta < 1^\circ$ has a finite frequency at the Γ point and a dispersion flat enough to show visible contribution [see Fig. 5(a)]. For larger twist angels, the contribution at low frequency belongs to the ZA branch, which reaches higher energy values as the angle increases. The two peaks at $75\,\mathrm{cm}^{-1}$ and $80\,\mathrm{cm}^{-1}$ belong to the breathing mode, which after an avoided crossing with the acoustic modes, splits into two branches visible in the projected band structure. The difference between the relaxed and the rigid calculation is more evident when projecting onto the central Γ point. It is clear how the imaginary frequency shear mode contributions to the PDOS are largely reduced in the relaxed case. The relaxation also effects the width of the avoided crossing with the LBMs: The coupling to neighboring Γ points broadens the LBMs, while relaxation at very small twist angles narrows them again.

It is instructive here to compare to the case of TMD bilayers, which feature a similar effect of the moiré. The position of the crossing between breathing and acoustic modes is determined (beyond the atomic weight of the constituent atoms) by two independent numbers: the slope of the acoustic branch (determined by the intralayer coupling) and the energy of the breathing mode of the pristine bilayer (related to the interlayer coupling). Due to the substantial difference in weight, the graphene breathing mode is substantially higher in frequency, and the velocity of sound (i.e., the slope of the acoustic branches) is larger. For bilayer graphene, the crossing thus occurs at twist angles of around two degrees (as opposed to roughly four degrees in MoS_2), i.e., at a much larger size of the moiré superstructure. As a consequence, the variations in interlayer spacing are much larger, and the effect of lattice relaxation is stronger for graphene, as apparent through the much wider spread of the breathing mode frequencies in tBLG.

IV. CONCLUSIONS

In conclusion, we have presented a reciprocal-space model for describing moiré-induced modifications of the phonon

band structure of twisted homobilayers. Our model includes the relaxation of the lattice, using a membrane model, as well as the full coupling between all backfolded phonon branches. We identify an avoided crossing between the layer breathing mode and the acoustic modes, that should be present for most homobilayers—at a specific twist angle determined by the breathing mode frequency and the slope of the acoustic branches (speed of sound). We apply our model to twisted bilayer graphene, and investigate in detail the evolution of the phonon density of states with twist angle. Indeed, we find strong modulation of the phonon density of states with twist angle around $\theta \approx 2^\circ$ where the avoided crossing occurs: A broad peak emerges when the backfolded acoustic modes become degenerate with the layer breathing mode at Γ. We expect the same qualitative behavior for other homobilayers, allowing for the targeted tailoring also of phononic properties by suitable twisting. In particular, a suitable combination of material parameters could yield a bilayer where avoided crossings in the electronic and phononic band structures appear at similar twist angle, opening the door for interesting electron-phonon coupling.

ACKNOWLEDGMENTS

The authors gratefully acknowledge support by the Austrian Science Fund FWF (D-A-CH Project I 3827-N36) and the Doctoral College TU-D funded by TU Wien. N.G. acknowledges financial support from the Croatian Science Foundation (Grant No. UIP-2019-04-6869).

APPENDIX A: MATHEMATICAL DERIVATION AND ELEMENTS OF THE MOIRÉ DYNAMICAL MATRIX

Phonon band structures are typically calculated in the harmonic approximation by expanding the total potential energy to second order in the atomic displacements. Phonon energies are then given as the eigenvalues of the dynamical matrix $\overline{\mathrm{D}}$. In the following, we present two complementary derivations of our formalism. We will first consider the dynamical matrix of a pristine bilayer unit cell, with an additional variation of force constants caused by the moiré lattice. This spatial dependence breaks translational invariance when going from one bilayer unit cell to the next. As a consequence, the associated dynamical matrix becomes nondiagonal in reciprocal space. In a second derivation, we focus directly on the dynamical matrix of the full moiré supercell in real space. We show that both approaches ultimately lead to the same expression—considering both provides valuable insights into the approximations employed.

1. Non diagonal dynamical matrix in momentum space

Consider the dynamical matrix for a pristine bilayer (BL),

$$D^{\mathrm{BL}}(\mathbf{q})_{\alpha,\alpha'} = \frac{1}{\sqrt{M_j M'_j}} \sum_{\mathbf{R}-\mathbf{R}'} e^{i\mathbf{q}\mathbf{R}} C_{j,j'}(\mathbf{R}-\mathbf{R}') e^{-i\mathbf{q}\mathbf{R}'}. \quad \text{(A1)}$$

Indices α, α' run over the $3n$ degrees of freedom in each pristine unit cell with n atoms. Lattice vectors $\mathbf{R}$ and $\mathbf{R}'$ run over the pristine unit cells. The entries of $\overline{D}$ are the Fourier transforms of the Hessians $\overline{C}$ containing the interatomic force constants. In a Bloch periodic system, interatomic force constants only depend on the relative position of the two unit cells, $\mathbf{R_p} - \mathbf{R_{p'}}$. However, in the twisted bilayer system, the relative local stacking $\mathbf{d}(\mathbf{r})$ changes as a function of position within the moiré supercell, resulting in an additional position dependence. We consider here the case where the twist angle is small ($\theta < 10^\circ$) and the moiré supercell is large. In this case, the gradual change of the geometry with local stacking leads to a slow, smooth variation of the $C_{\alpha,\alpha'}$ in real space when going from one pristine bilayer unit cell to the next. We can map the unit cell positions $\mathbf{R}$ within the moiré supercell onto the relative local stacking $\mathbf{d}((\mathbf{R}+\mathbf{R}')/2) \approx \mathbf{d}(\langle\mathbf{R}\rangle)$—we can then evaluate the forces at the appropriate stacking,

$$C_{\alpha,\alpha'}(\mathbf{R}-\mathbf{R}'|\mathbf{d}(\langle\mathbf{R}\rangle)) = \frac{\partial^2 V(\mathbf{d})}{\partial \mathbf{r}_\alpha \partial \mathbf{r}_{\alpha'}}, \quad \text{(A2)}$$

where $V(\mathbf{d})$ denotes the potential energy surface at a given local stacking $\mathbf{d}$. Due to its importance, we denote the additional local dependence of the force constants on position after a "|" in Eq. (A2)—this dependence breaks translational invariance of Eq. (A1), leading to a nondiagonal dynamical matrix in momentum space for a moiré (m),

$$D^m_{\alpha,\alpha'}(\mathbf{q},\mathbf{q}') = \frac{1}{\sqrt{M_\alpha M_{\alpha'}}} \cdot \sum_{\mathbf{R},\mathbf{R}'} e^{i\mathbf{R}\mathbf{q}} C_{\alpha,\alpha'} \times (\mathbf{R}-\mathbf{R}'|\mathbf{d}(\langle\mathbf{R}\rangle)) e^{-i\mathbf{R}'\mathbf{q}'}. \quad \text{(A3)}$$

Wavevectors $\mathbf{q}$ and $\mathbf{q}'$ belong to the small moiré BZ, while the vector $\mathbf{d}(\mathbf{R_p})$ belongs to configuration space. The goal is now to simplify the real-space positional dependence. The first step is to make use of the moiré periodicity of the twist angle induced displacement vector $\mathbf{d}$, which for a small twist angle Θ can be obtained as $-\Theta\hat{z} \times \mathbf{R}$ when using the usual small angle approximations [$\sin(\Theta) \approx \Theta$ and $\cos(\Theta) \approx 1$]. Vector $\mathbf{d}$ is periodic with the moiré period $\mathbf{d}(\mathbf{R}) \approx \mathbf{d}(\mathbf{R}+\mathbf{L}_M)$. Since the size of the pristine unit cell and moiré unit cell are related via $\mathbf{a} = \Theta\hat{z} \times \mathbf{L}_M$, the second term in $\mathbf{d}(\mathbf{R}+\mathbf{L}_M) = -\Theta\hat{z} \times (\mathbf{R}+\mathbf{L}_M)$ simplifies to $\mathbf{a}$. Therefore, one can expand $C_{\alpha,\alpha'}$ in terms of pristine reciprocal lattice vectors $\mathbf{G}$,

$$C_{\alpha,\alpha'}(\mathbf{R}-\mathbf{R}'|\mathbf{d}) = \sum_{\mathbf{G}} C_{\alpha,\alpha'}(\mathbf{R}-\mathbf{R}'|\mathbf{G}) e^{-i\mathbf{d}\mathbf{G}}. \quad \text{(A4)}$$

Note that vector $\mathbf{d}$ belongs to configuration space and $\mathbf{G}$ to its Fourier transform. This rewrite is useful if the $C_{\alpha,\alpha'}(\mathbf{R}-\mathbf{R}'|\mathbf{d})$ vary sufficiently slowly in space as to represent a reasonably smooth function—we find this to be true numerically; indeed, a 10×10 grid of DFPT calculations provides enough data to interpolate the $\mathbf{d}$ dependence.

Introducing $\mathbf{R}'' = \mathbf{R} - \mathbf{R}'$, Eq. (A3) can be written as

$$D^m_{\alpha,\alpha'}(\mathbf{q},\mathbf{q}') = \frac{1}{\sqrt{M_\alpha M_{\alpha'}}} \cdot \sum_{\mathbf{R},\mathbf{R}'',\mathbf{G}} C_{\alpha,\alpha'}(\mathbf{R}''|\mathbf{G}) \times e^{-i\mathbf{d}\mathbf{G}} e^{i\mathbf{R}''\mathbf{q}'} e^{i\mathbf{R}(\mathbf{q}-\mathbf{q}')}. \quad \text{(A5)}$$

The product $\mathbf{d}\cdot\mathbf{G}$ can be rewritten in terms of the moiré reciprocal lattice vectors $\tilde{\mathbf{G}}$,

$$\mathbf{d}\cdot\mathbf{G} = -\Theta\hat{z} \times \mathbf{R}\cdot\mathbf{G} = \Theta\hat{z} \times \mathbf{G}\cdot\mathbf{R} = \tilde{\mathbf{G}}\cdot\mathbf{R}. \quad \text{(A6)}$$

Equation (A14) then becomes

$$D^m_{\alpha,\alpha'}(\mathbf{q},\mathbf{q}') = \sum_{\mathbf{R},\mathbf{G}} e^{i\mathbf{R}(\mathbf{q}-\mathbf{q}'-\tilde{\mathbf{G}})} \cdot \underbrace{\frac{1}{\sqrt{M_\alpha M_{\alpha'}}} \sum_{\mathbf{R}''} C_{\alpha,\alpha'}(\mathbf{R}''|\mathbf{G}) e^{i\mathbf{R}''\mathbf{q}'}}_{D_{\alpha,\alpha'}(\mathbf{q}'|\mathbf{G})}. \quad \text{(A7)}$$

Finally, we can recognize the standard expression for a dynamical matrix in a Bloch periodic system, with an additional $\mathbf{G}$ dependence, which we denote again using the "|" symbol. We thus obtain an expression for the moiré dynamical matrix elements

$$D^m_{\alpha,\alpha'}(\mathbf{q},\mathbf{q}') = \sum_{\mathbf{R},\mathbf{G}} e^{i\mathbf{R}(\mathbf{q}-\mathbf{q}'-\tilde{\mathbf{G}})} D_{\alpha,\alpha'}(\mathbf{q}'|\mathbf{G}). \quad \text{(A8)}$$

The vertical bar between the vectors $\mathbf{G}$ and $\mathbf{q}'$ emphasizes that they represent variables in reciprocal configuration space and reciprocal moiré space respectively. The additional sum over unit cells $\mathbf{R}$ results in a delta function,

$$D^m_{\alpha,\alpha'}(\mathbf{q},\mathbf{q}') = \sum_{\mathbf{G}} \delta(\mathbf{q}-\mathbf{q}'-\tilde{\mathbf{G}}) D_{\alpha,\alpha'}(\mathbf{q}'|\mathbf{G}). \quad \text{(A9)}$$

The nondiagonal form of Eq. (A9) in $\mathbf{q}$ space still needs clarification: the δ function in Eq. (A9) ensures that $\mathbf{q}$ and $\mathbf{q}'$ are identical up to a reciprocal lattice vector $\tilde{\mathbf{G}}$. One can thus write the full dynamical matrix $\overline{D}^m(\mathbf{q})$ by explicitly introducing the reciprocal lattice vectors as matrix dimensions, as written in Eq. (11). In such a way, we obtain a large matrix (with a corresponding large number of eigenvalues) accounting for the many backfolded branches of the phonon band structure of the large moiré supercell.

To construct the moiré dynamical matrix from a pristine dynamical matrices following Eqs. (A7) and (A4) we use a Fourier sum,

$$D_{\alpha,\alpha'}(\mathbf{q}'|\mathbf{G}) = \sum_{\mathbf{d}} D_{\alpha,\alpha'}(\mathbf{q}'|\mathbf{d}) e^{i\mathbf{d}\mathbf{q}'}. \quad \text{(A10)}$$

The Fourier sum over all the stacking combinations inside a large moiré unit cell yields an additional $\mathbf{q}'$ dependence. We perform the summation over a uniform mesh of $10 \times 10\,\mathbf{d}$ values. Note that relaxation effects warp the straightforward relation between $\mathbf{d}$ and $\mathbf{R}$, as discussed in the main text, Eq. (10).

We finally discuss the approximations used in the diagonal and off-diagonal entries of the matrix representation Eq. (11). In the small twist angle regime, we can evaluate Θ phonon frequencies close to the Γ point in moiré BZ neglecting the $\mathbf{q}$ dependence in the dynamical matrix $\overline{D}(\mathbf{G}|\mathbf{q})$ for $\mathbf{G} \gg \mathbf{q}$. The pristine reciprocal lattice vectors spanning a configuration space BZ are much larger in magnitude that the moiré reciprocal lattice vector $|\tilde{\mathbf{G}}| \ll |\mathbf{G}|$. This leaves only the $\mathbf{q}$ dependence along the diagonal of the model dynamical matrix. Also, one needs to truncate the sum over $\mathbf{G}$ vectors. $|D_{\kappa\alpha,\kappa'\alpha'}(\mathbf{G}|\mathbf{q}')|$ decays quickly with increasing $|\mathbf{G}|$ [52]. At large twist angles, we can approximate by cutting the expansion after the first shell of $\mathbf{G}$ points—see, e.g., in the first column of Fig. 4. The additional phonon bands one would obtain with a larger cutoff shell then only adds (near-)degenerate additional lines to the phonon band structure. However, for smaller angles, such an approach proves not accurate enough, due to the small size of the Brillouin zone more Γ points need to be considered. We then define an outer cutoff, which is denoted by a black circle in Fig. 1(g) and clearly varies with the twist angle (see Fig. 2). Its diameter is defined by the condition that it must not be larger than the pristine reciprocal unit vector, while it progressively includes more neighboring $\tilde{\mathbf{\Gamma}}$ point shells. All of the moiré $\tilde{\mathbf{G}}$ points, which fit inside it, define and enlarge the dimension of the moiré dynamical matrix via a pristine $\mathbf{G}$ cutoff ($\mathbf{G}$ and $\tilde{\mathbf{G}}$ are connected by $\tilde{\mathbf{G}} \approx \Theta\hat{z} \times \mathbf{G}$). The inner cutoff refers to the coupling between neighboring $\tilde{\mathbf{G}}$ points as denoted by red shaded hexagons in Fig. 1. An inner cutoff of one implies coupling of only one $\tilde{\mathbf{G}}$ to the first shell of its neighbors. The inner cutoff limits the off-diagonal elements in the moiré dynamical matrix. Not all of them are listed in Eq. (11) of the main text for brevity. For example, coupling between $\tilde{\mathbf{G}}_1$ as the central $\tilde{\mathbf{G}}$ point and its neighboring shell, i.e., $\tilde{\mathbf{G}}_2$ would be described by $\overline{D}(\tilde{\mathbf{G}}_1|\mathbf{G}_2)$. We also neglect the $\mathbf{q}'$ dependence in these terms.

2. Moiré dynamical matrix in real space

To better elucidate the relation between the full, exact dynamical matrix of the moiré superstructure and the momentum space representation of Eq. (11), we present an alternate derivation that initially considers the large real-space moiré supercell. The dynamical matrix of the entire moiré is, of course, much larger: We now consider $p = 1, \ldots, n_c$ pristine unit cells that form the supermoiré unit cell, with n atoms per pristine unit cell and a total of $N = n_c \times n$ atoms in the moiré supercell. The full dynamical matrix is thus of size $3N \times 3N$, and thus prohibitively large to calculate. It can be written as

$$D^m_{p\alpha,p'\alpha'}(\mathbf{q}) = \frac{1}{\sqrt{M_\alpha M_{\alpha'}}} \cdot \sum_{L_m} e^{i\mathbf{R}_{p\mathbf{q}}} C_{p\alpha,p'\alpha'}(L_m) e^{-i\mathbf{R}_{\mathbf{L_m},p'}\mathbf{q}}. \quad \text{(A11)}$$

The spatial dependence of the force constants now appears explicitly as the p-dependence of the full Hessian matrix of the moiré, $C_{p\alpha,p'\alpha'}$. We explicitly add the Bloch phases for each unit cell (as opposed to just going from one moiré supercell to the next) for easier comparison with the momentum-space based derivation above. An additional phase will appear for the small number of interactions between atoms in different moiré supercells, written as the sum over the moiré lattice vectors L_m above. Note that we do not sum over the unit cells within the moiré in Eq. (A11), as p, p' now explicitly appear as matrix indices.

As before, we want to exploit the slow variation of the local stacking within the moiré. More specifically, the large $\overline{D}^m$ matrix consists of a repetition of almost, but not exactly, identical blocks due to the slow spatial modulation of the coupling within the moiré. Such a pattern suggests a basis change to a Fourier basis for the unit cell indices p, p' for the matrix $\overline{D}^m$. Since we now explicitly consider the two positions p and p' as matrix indices, we can interpret the Fourier expansion of the $C_{p\alpha,p'\alpha'}$ as a basis transformation from position-basis into a reciprocal basis, with a transformation matrix

$$U_{p,g} = e^{i\mathbf{d}_p\mathbf{G}_g} \quad \text{(A12)}$$

TABLE I. Some examples of the twist angle and its corresponding cutoff magnitudes (see Fig. 7) and the full dimension of the dynamical matrix.

Θ	Outer cutoff	Dyn. matrix dimension
10°	3	444 × 444
5°	5	1092 × 1092
2°	16	9804 × 9804
1°	28	29244 × 29244
0.5°	57	119028 × 119028

where the g represent matrix indices in the basis of reciprocal lattice vectors,

$$C_{p\alpha,p'\alpha'} = \sum_{g,g'} U_{p,g} C_{g\alpha,g'\alpha'} U^{\dagger}_{g',p'}. \tag{A13}$$

At this point, we have merely performed a basis change from a position-basis indexed with p to a Fourier basis indexed by g. If all g are included, and all distances between layers are evaluated at the correct distances taken from the relaxed supercell, this basis change does not introduce any approximations. In practice, Eq. (A13) again constitutes a Fourier transform of the force constants, formally written as basis transformation.

Inserting the Fourier expansion (A13), Eq. (A11) can be written as

$$D^{m}_{\alpha p,\alpha' p'}(\mathbf{q}) = \sum_{g,g'} U_{p,g} \cdot \underbrace{\sum_{\mathbf{L_m}} \frac{1}{\sqrt{M_\alpha M_{\alpha'}}} C_{g\alpha,g'\alpha'} e^{i(\mathbf{R_p}-\mathbf{R'_p}\mathbf{L_m})}}_{D^{m}_{\alpha g,\alpha' g'}} U^{\dagger}_{g',p'}. \tag{A14}$$

Since the eigenvalues of a matrix are independent of the basis, we can now directly calculate the eigenvalues of $D^{m}_{g\alpha,g'\alpha'}$. The g, g' run over the reciprocal lattice vectors $\tilde{\mathbf{G}}_g$. For the off-diagonal elements, the $\tilde{\mathbf{G}}$ can be rewritten as $\mathbf{G}$ using Eq. (A6). Enumerating a few matrix elements then provides exactly the matrix structure as in Eq. (11).

It is instructive to consider the contribution of the different Fourier components of the Fourier expansion in Eq. (A13). If the force constants vary slowly with $\mathbf{d}$, as we have verified numerically, we can truncate the Fourier basis after a few terms, since the matrix elements for larger $\tilde{\mathbf{G}}_g$ will be zero anyway. Consequently, the basis change of the matrix D from configuration space to its Fourier transform vastly reduces the size of the problem at hand: While $D^{m}_{g\alpha,g'\alpha'}$ is formally still an $3N \times 3N$ matrix, we can consider only a small subset of the g, g' along the reciprocal lattice points closest to Γ, arriving precisely at the momentum-based matrix form for $\overline{D}^{m}$ of Eq. (11). Both approaches thus yield identical expressions. Indeed, the final size of the problem needed to be considered (see Table I) is precisely given by those terms in the Fourier transformation of the force constants, Eq. (A13) that still yield large contributions.

In the second formulation, we more explicitly approximate the moiré dynamical matrix, and use the Fourier transform of the force constants as a means to reduce the problem size. There are two approximations included here: Explicitly, we drop the Fourier contributions for large $\tilde{\mathbf{G}}_g$, as the force constants vary sufficiently smoothly as a function of $\mathbf{d}$ to be well represented by a few Fourier components. Implicitly, we have to evaluate the force constants for a specific vertical distance—which might not be the correct vertical distance inside the moiré when including relaxation effects. We discuss the implications of the latter approximation in Appendix C.

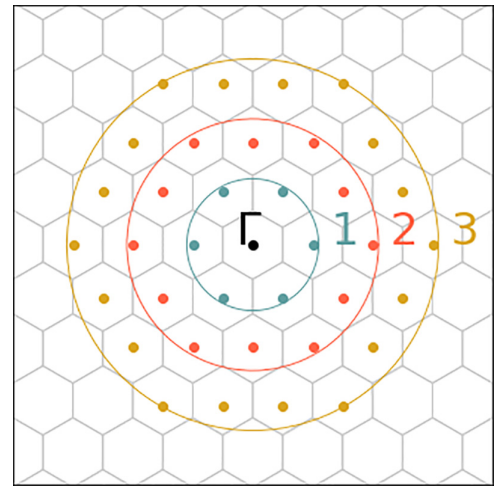

FIG. 7. Example of the variable outer cutoff with values 1, 2, 3.

The dynamical matrix dimension grows rapidly as the angle decreases. Since each Γ point only interacts with its neighbors, the resulting matrix structure is quite sparse, making the calculation computationally feasible.

APPENDIX B: PDOS CONTRIBUTIONS FROM ONLY THE FIRST $\tilde{\mathbf{G}}$ SHELL

When cutting off the expansion after the first shell of $\tilde{\Gamma}$ points as in (11), we obtain the PDOS in Fig. 8. While for larger angles ($\Theta > 5°$), the two pictures (Figs. 6 and 8) almost coincide, it is for smaller angles that this approximation fails. If we focus first at frequencies $\omega \to 0$, contributions from only the first shell of $\tilde{\Gamma}$ points creates the ZA mode contribution, which parabolically, but slowly extends to larger frequencies as the angle Θ increases. In Fig. 6 the same happened at much lower values of the twist angle due to the heavier nuclei of the bilayer transition metal resulting in smaller phonon frequencies. The inclusion of a larger number of $\tilde{\mathbf{G}}$ point shells, allows the ZA mode to backfold more often, and its frequency thus reaches higher values. Probably the most striking effect in Fig. 8 is how narrow and modest the LBM becomes due to the smaller number of the off diagonal elements in the dynamical matrix, which broaden it. Although the largest PDOS contribution still belongs to the LBM due to its flat dispersion, a large part deriving from its backfolding and TA mode avoided crossings is clearly missing. However, one can in this case more easily see how the LBM in the relaxed case features one sharp maximum for the smallest twist angle, while in the rigid case there are three strong contributions. While the out-of-plane projection shows the same features as the full PDOS, we notice that the central Γ-point projection is actually not too far off from the full result (see Fig. 6), since projecting onto the central Γ point,

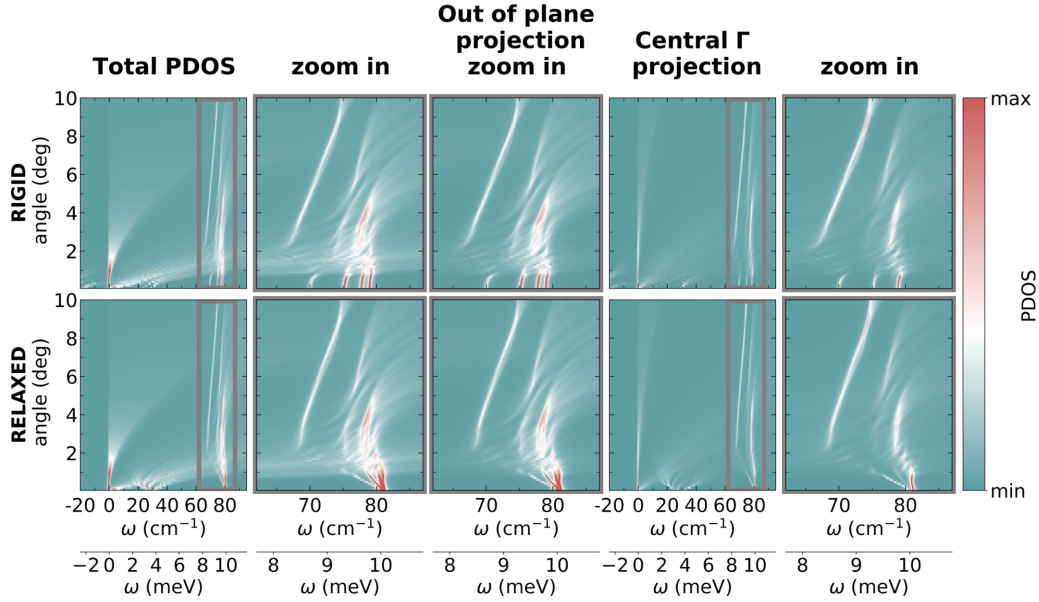

FIG. 8. Calculation with only the contributions from the first shell of neighboring $\tilde{\mathbf{G}}$ accounted for (outer cutoff = 1, see Fig. 7). In comparison with Fig. 6, a discontinuity happens at a much larger angle as the higher energy contributions become insufficient sooner, e.g., for $\omega \approx 50\ \mathrm{cm}^{-1}$ and $\Theta \approx 6^\circ$.

at low twist angles, misses a more complete dispersion from a smaller number of phonon modes.

APPENDIX C: RELAXED AND RIGID TWISTED BILAYER GRAPHENE

The effects of atomic relaxation become important for small twist angles (in our case $<2^\circ$), for which the real space unit cell is of considerable size. Although weak, van der Walls interlayer forces manage to outweigh the strong intralayer bonding, making the energetically favorable AB stacking take up a larger portion of the bilayer than it would for a simple rigid twist (see Fig. 9).

The relaxation-induced atomic displacement is obtained from the total energy of the series of DFT calculations, which sample the configuration space. In Fig. 3, the GSFE potential is mapped onto a pristine unit cell and describes the optimal position for the second layer on top of the first one. The minimum is achieved for AB stacking. Mathematically, the simplest form of the interlayer binding energy as a function of displacement $\mathbf{d}$ is proposed, which preserves its periodicity with the pristine unit cell,

$$U_B[\mathbf{u}_t, \mathbf{u}_b] = \int V[\mathbf{u}_t(r) - \mathbf{u}_b(r)]d^2\mathbf{r},$$
$$V[\mathbf{u}_t, \mathbf{u}_b] = \sum_G c_\mathbf{G} \cos((\mathbf{u}_t(r) - \mathbf{u}_b(r) + \mathbf{d}) \cdot \mathbf{G}), \tag{C1}$$

$c_\mathbf{G}$ are the Fourier coefficients of GSFE in reciprocal space. Since (C1) depends on the relaxation and twist angle induced relative displacement of the two layers, one needs to solve the relaxation problem self-consistently, by total energy functional minimization (8).

APPENDIX D: THE ROLE OF CORRUGATION

While our theory works well for the evolution of the breathing modes, and the associated crossings with the acoustic branches, we find our calculations incorrectly predict an imaginary shear mode frequency at intermediate twist angles. To elucidate the cause, we note that we neglect the dependence

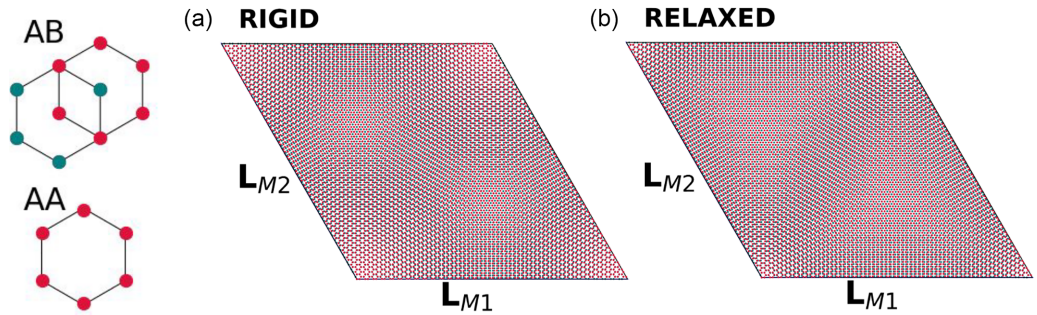

FIG. 9. Difference between the rigid (a) and relaxed (b) real-space tBLG structure at $\Theta = 1.018^\circ$. Schematics on the left show the typical AA and AB stackings. In the relaxed regime, the AB stacking dominates the super cell.

of the corrugation amplitude on twist angle. For small twist angles (relaxed regime), the various stacking regions [AA vs AB(BA)] can be viewed as completely independent. AA as well as AB(BA) stacking configurations are approximately at their equilibrium layer separation [73] ($\Delta AA \approx 3.53$ Å and $\Delta AB \approx 3.33$ Å). In the transition regime (with increased twist angle, i.e., reduced super cell size), the stacking configurations move closer to each other. Therefore, the corrugation $\Delta = \Delta AA - \Delta AB$ is reduced and the layer separation becomes more uniform, $\Delta AA \approx \Delta AB \approx 3.33$ Åin the large angle limit. This is not accounted for by the assembled dynamical matrix, as we compute each local stacking at its equilibrium distance. Including this effect, i.e., a reduced corrugation, would cause ΔAA to decrease and ΔAB to increase. These changes increase the differences in generalized stacking fault energies (GSFE) between the AA and AB regions due to its exponential sensitivity on layer separation. A larger GSFE difference will increase strain in the system. This contribution will shift the point at which the relative weight of the AB(BA) area starts to decline to a larger twist angle, causing the shear mode to stay approximately constant up to a larger twist angle. By contrast, without considering the effect of reduced corrugation at intermediate twist angles on the GSFE, the S mode frequency starts to decrease at a smaller twist angle due to the decrease of the relative weight of the AB regions as seen in our calculations.

[1] R. Bistritzer and A. H. MacDonald, Moiré bands in twisted double-layer graphene, Proc. Natl. Acad. Sci. USA **108**, 12233 (2011).

[2] A. K. Geim and I. V. Grigorieva, van der Waals heterostructure, Nature (London) **499**, 419 (2013).

[3] K. Novoselov, A. K. Geim, S. V. Morozov, D. Jiang, Y. Zhang, S. V. Dubonos, I. V. Grigorieva, and A. A. Firsov, Electronic field effect in atomically thin carbon films, Science **306**, 666 (2004).

[4] K. S. Novoselov, A. Mishchenko, A. Carvalho, and A. H. Castro Neto, 2d materials and van der Waals heterostructures, Science **353**, aac9439 (2016).

[5] Y. Cao, V. Fatemi, S. Fang, K. Watanabe, T. Taniguchi, E. Kaxiras, and P. Jarillo-Herrero, Unconventional superconductivity in magic-angle graphene superlattices, Nature (London) **556**, 43 (2018).

[6] T. I. Andersen, G. Scuri, A. Sushko, K. De Greve, J. Sung, Y. Zhou, D. S. Wild, R. J. Gelly, H. Heo, K. Watanabe *et al.*, Moiré excitons correlated with superlattice structure in twisted WSe_2/WSe_2 homobilayers, Nat. Mater. **20**, 480 (2021).

[7] F. Guinea and N. R. Walet, Continuum models for twisted bilayer graphene: The effects of lattice deformation and hopping parameter, Phys. Rev. B **99**, 205134 (2019).

[8] X. Li, F. Wu, and A. H. MacDonald, Electronic structure of single-twist trilayer graphene, arXiv:1907.12338.

[9] I. Maity, M. H. Naik, P. K. Maiti, H. R. Krishnamurthy, and M. Jain, Phonons in twisted transition-metal dichalcogenide bilayer: Ultrasoft phasons and a transition from a superlubric to a pinned phase, Phys. Rev. Res. **2**, 013335 (2020).

[10] A. Weston, Y. Zou, V. Enaldiev, A. Summerfield, N. Clark, V. Z'olyomi, A. Graham, C. Yelgel, S. Magorrian, M. Zhou *et al.*, Atomic reconstruction in twisted bilayers of transition metal dichalcogenides, Nat. Nanotechnol. **15**, 592 (2020).

[11] H. Yoo, R. Engelke, S. Carr, S. Fang, K. Zhang, P. Cazeaux, S. H. Sung, R. Hovden, A. W. Tsen, T. Taniguchi *et al.*, Atomic and electronic reconstruction at the van der Waals interface in twisted bilayer graphene, Nat. Mater. **18**, 448 (2019).

[12] K. L. Seyle, P. Rivera, H. Yu, N. P. Wilson, E. L. Ray, D. Mandrus, J. Yan, W. Yao, and X. Xu, Signatures of moiré-trapped valley excitons in $MoSe_2/WSe_2$ heterostructures, Nature (London) **567**, 66 (2019).

[13] Y. Cao, V. Fatemi, A. Demir, S. Fang, S. L. Tomarken, J. Y. Luo, J. D. Sanchez-Yamagishi, K. Watanabe, T. Taniguchi, E. Kaxiras *et al.*, Correlated insulator behaviour at half-filling in magic-angle graphene superlattices, Nature (London) **556**, 80 (2018).

[14] P. Stepanov, I. Das, X. Lu, A. Fahimniya, K. Watanabe, T. Taniguchi, F. H. L. Koppens, J. Lischner, L. Levitov, and D. K. Efetov, Untying the insulating and superconducting orders in magic-angle graphene, Nature (London) **583**, 375 (2020).

[15] M. Yankowitz, S. Chen, H. Polshyn, Y. Zhang, K. Watanabe, T. Taniguchi, D. Graf, A. F. Young, and C. R. Dean, Tuning superconductivity in twisted bilayer graphene, Science **363**, 1059 (2019).

[16] C. Xu and L. Balents, Topological superconductivity in twisted multilayer graphene, Phys. Rev. Lett. **121**, 087001 (2018).

[17] H. C. Po, L. Zou, A. Vishwanath, and T. Senthil, Origin of Mott insulating behavior and superconductivity in twisted bilayer graphene, Phys. Rev. X **8**, 031089 (2018).

[18] H. Isobe, N. F. Q. Yuan, and L. Fu, Unconventional superconductivity and density waves in twisted bilayer graphene, Phys. Rev. X **8**, 041041 (2018).

[19] D. M. Kennes, J. Lischner, and C. Karrasch, Strong correlations and $d + id$ superconductivity in twisted bilayer graphene, Phys. Rev. B **98**, 241407(R) (2018).

[20] J. F. Dodaro, S. A. Kivelson, Y. Schattner, X. Q. Sun, and C. Wang, Phases of a phenomenological model of twisted bilayer graphene, Phys. Rev. B **98**, 075154 (2018).

[21] Y.-P. Lin and R. M. Nandkishore, Kohn-luttinger superconductivity on two orbital honeycomb lattice, Phys. Rev. B **98**, 214521 (2018).

[22] Y. Sherkunov and J. J. Betouras, Electronic phases in twisted bilayer graphene at magic angles as a result of Van Hove singularities and interactions, Phys. Rev. B **98**, 205151 (2018).

[23] C.-C. Liu, L.-D. Zhang, W.-Q. Chen, and F. Yang, Chiral spin density wave and $d + id$ superconductivity in the magic-angle-twisted bilayer graphene, Phys. Rev. Lett. **121**, 217001 (2018).

[24] B. Roy and V. Juričić, Unconventional superconductivity in nearly flat bands in twisted bilayer graphene, Phys. Rev. B **99**, 121407(R) (2019).

[25] J. González and T. Stauber, Kohn-Luttinger superconductivity in twisted bilayer graphene, Phys. Rev. Lett. **122**, 026801 (2019).

[26] Y. Wang, J. Kang, and R. M. Fernandes, Topological and nematic superconductivity mediated by ferro-SU(4) fluctuations in twisted bilayer graphene, Phys. Rev. B **103**, 024506 (2021).
[27] Z. Hao, A. M. Zimmermann, P. Ledwith, E. Khalaf, D. Haie Najafabadi, K. Watanabe, T. Taniguchi, A. Vishwanath, and P. Kim, Electric field-tunable superconductivity in alternating-twist magic-angle trilayer graphene, Science **371**, 1133 (2021).
[28] J. M. Park, Y. Cao, K. Watanabe, T. Taniguchi, and P. Jarillo-Herrero, Tunable strongly coupled superconductivity in magic-angle twisted trilayer graphene, Nature (London) **590**, 249 (2021).
[29] L. Balents, C. R. Dean, D. K. Efetov, and A. F. Young, Superconductivity and strong correlations in moiré flat bands, Nat. Phys. **16**, 725 (2020).
[30] L. Zhang, Y. Wang, R. Hu, P. Wan, O. Zheliuk, M. Liang, X. Peng, Y.-J. Zeng, and J. Ye, Correlated states in strained twisted bilayer graphenes away from the magic angle, Nano Lett. **22**, 3204 (2022).
[31] L. Rademaker and P. Mellado, Charge-transfer insulation in twisted bilayer graphene, Phys. Rev. B **98**, 235158 (2018).
[32] A. Thomson, S. Chatterjee, S. Sachdev, and M. S. Scheurer, Triangular antiferromagnetism on the honeycomb lattice of twisted bilayer graphene, Phys. Rev. B **98**, 075109 (2018).
[33] J. W. F. Venderbos and R. M. Fernandes, Correlations and electronic order in a two-orbital honeycomb lattice model for twisted bilayer graphene, Phys. Rev. B **98**, 245103 (2018).
[34] J. Pizarro, M. Calderon, and E. Bascones, The nature of correlations in the insulating states of twisted bilayer graphene, J. Phys. Commun. **3**, 035024 (2019).
[35] J. Kang and O. Vafek, Non-abelian dirac node braiding and near-degeneracy of correlated phases at odd integer filling in magic-angle twisted bilayer graphene, Phys. Rev. B **102**, 035161 (2020).
[36] A. L. Sharpe, E. J. Fox, A. W. Barnard, J. Finney, K. Watanabe, T. Taniguchi, M. A. Kastner, and D. Goldhaber-Gordon, Evidence of orbital ferromagnetism in twisted bilayer graphene aligned to hexagonal boron nitride, Nano Lett. **21**, 4299 (2021).
[37] T. Huang, L. Zhang, and T. Ma, Antiferromagnetically ordered Mott insulator and d+id superconductivity in twisted bilayer graphene: A quantum Monte Carlo study, Sci. Bull. **64**, 310 (2019).
[38] J. Kang and O. Vafek, Strong coupling phases of partially filled twisted bilayer graphene narrow bands, Phys. Rev. Lett. **122**, 246401 (2019).
[39] K. Seo, V. N. Kotov, and B. Uchoa, Ferromagnetic Mott state in twisted graphene bilayers at the magic angle, Phys. Rev. Lett. **122**, 246402 (2019).
[40] C. Repellin, Z. Dong, Y.-H. Zhang, and T. Senthil, Ferromagnetism in narrow bands of moiré superlattices, Phys. Rev. Lett. **124**, 187601 (2020).
[41] H. Ochoa and R. M. Fernandes, Degradation of phonons in disordered moiré superlattices, Phys. Rev. Lett. **128**, 065901 (2022).
[42] J. M. B. Lopes dos Santos, N. M. R. Peres, and A. H. Castro Neto, Graphene bilayer with a twist: Electronic structure, Phys. Rev. Lett. **99**, 256802 (2007).
[43] K. Hejazi, C. Liu, H. Shapourian, X. Chen, and L. Balents, Multiple topological transitions in twisted bilayer graphene near the first magic angle, Phys. Rev. B **99**, 035111 (2019).
[44] L. Classen, C. Honerkamp, and M. M. Scherer, Competing phases of interacting electrons on triangular lattices in moiré heterostructures, Phys. Rev. B **99**, 195120 (2019).
[45] B. Lian, Z. Wang, and B. A. Bernevig, Twisted bilayer graphene: A phonon-driven superconductor, Phys. Rev. Lett. **122**, 257002 (2019).
[46] F. Wu, A. H. MacDonald, and I. Martin, Theory of phonon-mediated superconductivity in twisted bilayer graphene, Phys. Rev. Lett. **121**, 257001 (2018).
[47] S. Carr, S. Fang, and E. Kaxiras, Electronic-structure methods for twisted moiré layers, Nat. Rev. Mater. **5**, 748 (2020).
[48] M. Koshino and Y.-W. Son, Moiré phonons in twisted bilayer graphene, Phys. Rev. B **100**, 075416 (2019).
[49] H. Ochoa, Moiré-pattern fluctuations and electron-phason coupling in twisted bilayer graphene, Phys. Rev. B **100**, 155426 (2019).
[50] Q. Gao and E. Khalaf, Symmetry origin of lattice vibration modes in twisted multilayer graphene: Phasons versus moiré phonons, Phys. Rev. B **106**, 075420 (2022).
[51] R. Samajdar, Y. Teng, and M. S. Scheurer, Moiré phonons and impact of electronic symmetry breaking in twisted trilayer graphene, Phys. Rev. B **106**, L201403 (2022).
[52] J. Quan, L. Linhart, M.-L. Lin, D. Lee, J. Zhu, C.-Y. Wang, W.-T. Hsu, J. Choi, J. Embley, C. Young *et al.*, Phonon renormalization in reconstructed MOS_2 moiré superlattices, Nat. Mater. **20**, 1100 (2021).
[53] J. Zang, J. Wang, J. Cano, and A. J. Millis, Hartree-fock study of the moiré Hubbard model for twisted bilayer transition metal dichalcogenides, Phys. Rev. B **104**, 075150 (2021).
[54] J. González and T. Stauber, Marginal fermi liquid in twisted bilayer graphene, Phys. Rev. Lett. **124**, 186801 (2020).
[55] M. Xie and A. H. MacDonald, Nature of the correlated insulator states in twisted bilayer graphene, Phys. Rev. Lett. **124**, 097601 (2020).
[56] P. Lucignano, D. Alfé, V. Cataudella, D. Ninno, and G. Cantele, Crucial role of atomic corrugation on the flat bands and energy gaps of twisted bilayer graphene at the magic angle $\theta \approx 1.08^\circ$, Phys. Rev. B **99**, 195419 (2019).
[57] N. N. T. Nam and M. Koshino, Lattice relaxation and energy band modulation in twisted bilayer graphene, Phys. Rev. B **96**, 075311 (2017).
[58] F. Wu, T. Lovorn, E. Tutuc, I. Martin, and A. H. MacDonald, Topological insulators in twisted transition metal dichalcogenide homobilayers, Phys. Rev. Lett. **122**, 086402 (2019).
[59] J. Jung, A. Raoux, Z. Qiao, and A. H. MacDonald, *Ab initio* theory of moiré superlattice bands in layered two-dimensional materials, Phys. Rev. B **89**, 205414 (2014).
[60] W.-T. Hsu, J. Quan, C.-R. Pan, P.-J. Chen, M.-Y. Chou, W.-H. Chang, A. H. MacDonald, X. Li, J.-F. Lin, and C.-K. Shih, Quantitative determination of interlayer electronic coupling at various critical points in bilayer MoS_2, Phys. Rev. B **106**, 125302 (2022).
[61] "quasi" in the sense that an arbitrary twist angle will in general not yield a moiré supercell commensurate with the periodicity of the honeycomb lattice.
[62] G. Kresse and J. Hafner, *Ab initio* molecular dynamics for liquid metals, Phys. Rev. B **47**, 558 (1993).
[63] G. Kresse and J. Hafner, Ab initio molecular-dynamics simulation of the liquid-metal-amorphous-semiconductor transition in germanium, Phys. Rev. B **49**, 14251 (1994).

[64] M. Gajdoš, K. Hummer, G. Kresse, J. Furthmüller, and F. Bechstedt, Linear optical properties in the projector-augmented wave methodology, Phys. Rev. B **73**, 045112 (2006).

[65] J. S. Alden, A. W. Tsen, P. Y. Huang, R. Hovden, L. Brown, J. Park, D. A. Muller, and P. L. McEuen, Strain solitons and topological defects in bilayer graphene, Proc. Natl. Acad. Sci. USA **110**, 11256 (2013).

[66] C. R. Woods, L. Britnell, A. Eckmann, R. S. Ma, J. C. Lu, H. M. Guo, X. Lin, G. L. Yu, Y. Cao, R. Gorbachev *et al.*, Commensurate-incommensurate transition in graphene on hexagonal boron nitride, Nat. Phys. **10**, 451 (2014).

[67] K. Zhang and E. B. Tadmor, Structural and electron diffraction scaling of twisted graphene bilayers, J. Mech. Phys. Solids **112**, 225 (2018).

[68] T. Fabian, M. Kausel, L. Linhart, J. Burgdörfer, and F. Libisch, Half-integer Wannier diagram and Brown-Zak fermions of graphene on hexagonal boron nitride, Phys. Rev. B **106**, 165412 (2022).

[69] S. Carr, D. Massatt, S. B. Torrisi, P. Cazeaux, M. Luskin, and E. Kaxiras, Relaxation and domain formation in incommensurate two-dimensional heterostructures, Phys. Rev. B **98**, 224102 (2018).

[70] J. Jung, E. Laksono, A. M. DaSilva, A. H. MacDonald, M. Mucha-Kruczyński, and S. Adam, Moiré band model and band gaps of graphene on hexagonal boron nitride, Phys. Rev. B **96**, 085442 (2017).

[71] R. He, T.-F. Chung, C. Delaney, C. Keiser, L. A. Jauregui, P. M. Shand, C. C. Chancey, Y. Wang, J. Bao, and Y. P. Chen, Observation of low energy raman modes in twisted bilayer graphene, Nano Lett. **13**, 3594 (2013).

[72] J.-W. Jiang, B.-S. Wang, and T. Rabczuk, Acoustic and breathing phonon modes in bilayer graphene with moiré patterns, Appl. Phys. Lett. **101**, 023113 (2012).

[73] J. Jung, A. M. DaSilva, A. H. MacDonald, and S. Adam, Origin of band gaps in graphene on hexagonal boron nitride, Nat. Commun. **6**, 6308 (2015).